Molecular Cell

Article

Reversal of mitochondrial malate dehydrogenase 2 enables anaplerosis via redox rescue in respiration-deficient cells

Graphical abstract

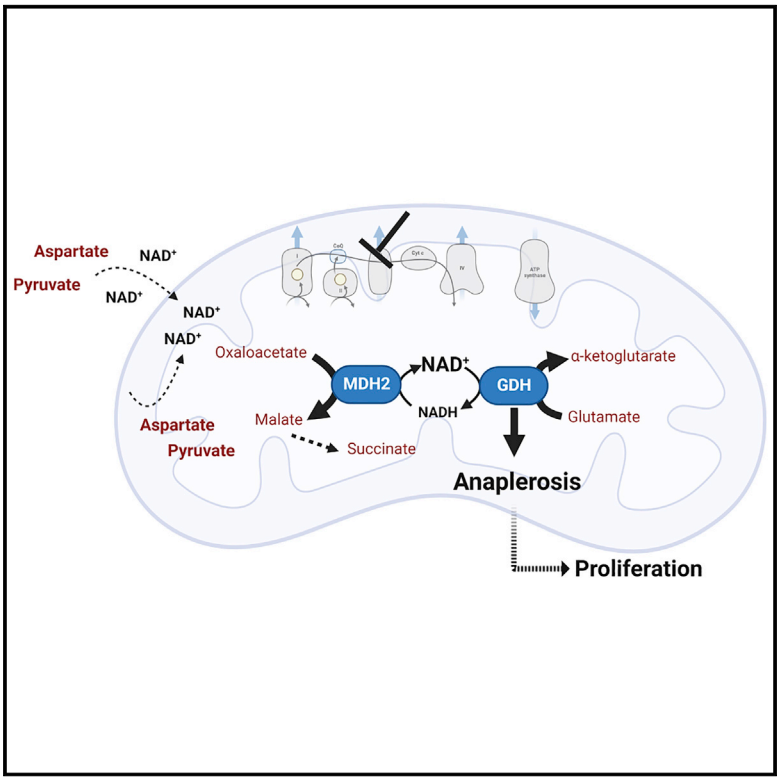

Highlights

- GDH is inhibited in ETC-deficient cells due to reduced mitochondrial NAD^+/NADH ratio
- Electron acceptors rescue mitochondrial redox defects via reversal of GOT2 and MDH2
- Reversed flux through MDH2 provides the NAD^+ required for GDH to mediate anaplerosis
- ETC deficiency and loss of MDH2 may be an effective combination for cancer therapy

Authors

Patricia Altea-Manzano, Anke Vandekeere, Joy Edwards-Hicks, ..., Sarah-Maria Fendt, Miguel Martin-Hernandez, Andrew J. Finch

Correspondence

miguelmartin@ugr.es (M.M.-H.), a.finch@qmul.ac.uk (A.J.F.)

In brief

Cancer cells show remarkable metabolic plasticity to overcome inhibition of respiration, limiting its efficacy in cancer therapy. Altea-Manzano et al. show that reversed flux through GOT2 and MDH2 rescues mitochondrial redox imbalance and supports cell viability by promoting NAD^+-dependent activity of GDH. Targeting MDH2 may complement therapeutic inhibition of respiration.

Altea-Manzano et al., 2022, Molecular Cell *82*, 4537–4547
December 1, 2022
https://doi.org/10.1016/j.molcel.2022.10.005

CellPress

Molecular Cell

CellPress
OPEN ACCESS

Article

Reversal of mitochondrial malate dehydrogenase 2 enables anaplerosis via redox rescue in respiration-deficient cells

Patricia Altea-Manzano,[1,2,3] Anke Vandekeere,[2,3,7] Joy Edwards-Hicks,[4,7] Mar Roldan,[1] Emily Abraham,[5] Xhordi Lleshi,[4] Ania Naila Guerrieri,[4] Domenica Berardi,[4] Jimi Wills,[4] Jair Marques Junior,[4] Asimina Pantazi,[4] Juan Carlos Acosta,[4,8] Rosario M. Sanchez-Martin,[1] Sarah-Maria Fendt,[2,3] Miguel Martin-Hernandez,[1,6,*] and Andrew J. Finch[4,5,9,*]

[1]GENYO, Centre for Genomics and Oncological Research, Pfizer/Universidad de Granada, Junta de Andalucía, Granada 18016, Spain
[2]Laboratory of Cellular Metabolism and Metabolic Regulation, VIB-KU Leuven Center for Cancer Biology, VIB, Leuven 3000, Belgium
[3]Laboratory of Cellular Metabolism and Metabolic Regulation, Department of Oncology, KU Leuven and Leuven Cancer Institute (LKI), Leuven 3000, Belgium
[4]Cancer Research UK Edinburgh Centre, Institute of Genetics and Cancer, University of Edinburgh, Crewe Road, Edinburgh EH4 2XR, UK
[5]Centre for Tumour Biology, Barts Cancer Institute, Queen Mary University of London, Charterhouse Square, London EC1M 6BQ, UK
[6]Biochemistry and Molecular Biology I Department, School of Sciences, University of Granada, Avda Fuentenueva, 18071 Granada, Spain
[7]These authors contributed equally
[8]Present address: Instituto de Biomedicina y Biotecnología de Cantabria, IBBTEC (CSIC, Universidad de Cantabria), C/Albert Einstein 22, Santander 39011, Spain
[9]Lead contact
*Correspondence: miguelmartin@ugr.es (M.M.-H.), a.finch@qmul.ac.uk (A.J.F.)
https://doi.org/10.1016/j.molcel.2022.10.005

SUMMARY

Inhibition of the electron transport chain (ETC) prevents the regeneration of mitochondrial NAD^+, resulting in cessation of the oxidative tricarboxylic acid (TCA) cycle and a consequent dependence upon reductive carboxylation for aspartate synthesis. NAD^+ regeneration alone in the cytosol can rescue the viability of ETC-deficient cells. Yet, how this occurs and whether transfer of oxidative equivalents to the mitochondrion is required remain unknown. Here, we show that inhibition of the ETC drives reversal of the mitochondrial aspartate transaminase (GOT2) as well as malate and succinate dehydrogenases (MDH2 and SDH) to transfer oxidative NAD^+ equivalents into the mitochondrion. This supports the NAD^+-dependent activity of the mitochondrial glutamate dehydrogenase (GDH) and thereby enables anaplerosis—the entry of glutamine-derived carbon into the TCA cycle and connected biosynthetic pathways. Thus, under impaired ETC function, the cytosolic redox state is communicated into the mitochondrion and acts as a rheostat to support GDH activity and cell viability.

INTRODUCTION

Many key metabolic pathways occur within mitochondria, and thus mitochondrial metabolism is an attractive target for development of anticancer therapeutic agents. The efficacy of the widely used anti-diabetic drug metformin in reducing cancer incidence in patients with diabetes (Decensi et al., 2010) and the identification of complex I of the electron transport chain (ETC) as one of its key targets (El-Mir et al., 2000; Owen et al., 2000; Wheaton et al., 2014) indicate that partial inhibition of mitochondrial respiration may be a well-tolerated and effective therapy. However, tumors are metabolically heterogeneous, and clonal emergence of cells that have adapted to inhibition of respiration poses a problem for such therapies.

Despite the pivotal roles of mitochondria in cell metabolism, various models have demonstrated that complete inhibition of respiration can be tolerated in cells. However, these models do reveal new metabolic dependencies caused by ETC disruption. For example, cells lacking mitochondrial DNA (termed "ρ^0 cells") have a requirement for pyruvate and uridine supplementation in their medium (King and Attardi, 1989). ETC-deficient cells need uridine to compensate for the activity of the pyrimidine biosynthesis enzyme dihydroorotate dehydrogenase (DHODH) that depends upon respiration (King and Attardi, 1989). The auxotrophic requirement for pyruvate in various ETC deficiency models was recently demonstrated to be due to its facilitation of aspartate biosynthesis (Birsoy et al., 2015; Cardaci et al., 2015; Lussey-Lepoutre et al., 2015; Sullivan et al., 2015). Indeed, supplementation of tissue culture medium with aspartate, in place of pyruvate, can rescue the viability of ETC-deficient cells. Thus, compensatory rewiring of cellular metabolism in

response to ETC inhibition creates vulnerabilities that can be targeted for therapeutic intervention based upon synthetic lethality (Zecchini and Frezza, 2017). The study of metabolic adaptations to perturbations of ETC function is therefore of clinical relevance.

Cells with defective ETC function are dependent upon glycolysis alone for the generation of ATP. A source of nicotinamide adenine dinucleotide hydrogen (NADH) oxidation is required to regenerate the nicotinamide adenine dinucleotide (NAD^+) consumed during glycolysis, and in the absence of ETC function, the cytosolic lactate dehydrogenase (LDH) provides this activity. Indeed, this is generally thought to be the sole function for the lactate-producing activity of LDH. Stimulation of cytosolic NAD^+ regeneration alone can rescue the viability of ETC-deficient cells, as evidenced by the support of viability afforded by α-ketobutyrate (α-KB) (Sullivan et al., 2015) or expression of a cytosolic water-forming NADH oxidase (Titov et al., 2016). Even though it is clear how cytosolic NAD^+ regeneration would rescue the energetic defect during ETC deficiency, the mechanism through which it rescues the biosynthetic defects (e.g., synthesis of aspartate) is unknown. Furthermore, it remains unknown whether this cytosolic change in redox balance is transferred into the mitochondrion, the original site of the redox defect.

Aspartate is a key cellular biosynthetic intermediate, and in addition to its role as a proteogenic amino acid, it is also required for nucleotide biosynthesis, both as an amine donor (releasing fumarate) in the synthesis of GMP from AMP and as a biosynthetic intermediate in pyrimidine synthesis. It is also a substrate of arginosuccinate synthase in the urea cycle (again leading to the production of fumarate). It is important to note that none of the reactions involving aspartate in these pathways involves a redox co-factor. However, aspartate is also involved in one of the key redox shuttles in mammalian cells (the malate-aspartate shuttle) that transfers redox equivalents between the cytosol and the mitochondrion. We therefore hypothesized that the rescue of viability of ETC-deficient cells by cytosolic electron acceptors (e.g., aspartate, pyruvate, α-KB, and *Lb*NOX) might involve the transfer of oxidized redox equivalents into the mitochondrion through reversal of the malate-aspartate shuttle. Furthermore, we hypothesized that this redox transfer may be critical under certain metabolic scenarios.

Here, we show that aspartate and pyruvate drive "reversed" carbon flux through mitochondrial malate (MDH2) and succinate dehydrogenases (SDH) in ETC-deficient cells. This demonstrates that the mitochondrial arm of the malate-aspartate shuttle can run in reverse to transfer oxidative equivalents from the cytosol into the mitochondrion. Furthermore, we show that the mitochondrial components of the shuttle are required for cytosolic NAD^+ regeneration to rescue viability, indicating that redox transfer between the two compartments is essential. Finally, we show that the oxidative equivalents transferred into the mitochondrion enable the activity of glutamate dehydrogenase (GDH) and thus permit the entry of glutamine-derived carbon into the tricarboxylic acid (TCA) cycle (anaplerosis), thereby supporting reductive carboxylation, aspartate generation, and rescue of cell viability.

RESULTS

Aspartate and pyruvate tracing show reductive metabolism in ETC-deficient cells

To gain insight into a possible involvement of redox metabolism in the rescue of viability upon respiration deficiency, we examined the roles of pyruvate and aspartate in the metabolic adaptations of cells lacking a functional mitochondrial ETC. Pyruvate can be converted to aspartate via the action of pyruvate carboxylase, yielding oxaloacetate, and subsequent transamination via aspartate aminotransferase activity. We assessed carbon transfer from pyruvate to aspartate using $^{13}C_3$-pyruvate tracing and observed aspartate (m + 3) that was abundant in both respiration-competent 143B cells and their respiration-defective ρ^0 counterparts (Figure 1A; Table S1), consistent with the key activity of pyruvate carboxylase in ETC-deficient cells as previously reported (Cardaci et al., 2015; Lussey-Lepoutre et al., 2015). This indicates that aspartate can be produced from pyruvate without involvement of enzymes requiring redox co-factors.

Rescue of respiration deficiency can also be achieved through cytosolic NAD^+ regeneration catalyzed by α-KB or through exogenous expression of a bacterial NADH oxygenase (Sullivan et al., 2015; Titov et al., 2016). We therefore sought to examine metabolic pathways involving NADH oxidation that might be involved in this rescue of cell viability. First, we examined the metabolism of aspartate using $^{13}C_4$-aspartate and mass spectrometric stable isotope tracing. Aspartate can be metabolized to fumarate in the purine nucleotide and urea cycles, pathways that do not involve redox co-factors. Aspartate can also be metabolized to malate and fumarate in both mitochondria and the cytosol by aspartate transaminases (GOTs) and malate dehydrogenases (MDHs), with the latter utilizing NAD^+/NADH as a co-factor. Thus, the mere presence of labeled carbon (m + 4) in fumarate and malate cannot distinguish which of these pathways were utilized, nor whether redox co-factors were involved. Of these three metabolic pathways, the GOT/MDH route from aspartate to fumarate is the only one that would be expected to be elevated in ρ^0 cells, due to the redox imbalance causing reversal of MDH. We observed malate (m + 4) and fumarate (m + 4) in both cell types, as expected, but there was a notable increase in the levels of these isotopologs in ρ^0 cells (Figure 1B; Table S2). To exclude respiration-independent effects of mtDNA depletion, we used antimycin A in parallel as an inhibitor of complex III of the ETC. Importantly, 143B cells treated with antimycin A showed a similar pattern of malate (m + 4) and fumarate (m + 4) accumulation to ρ^0 cells (Figure 1C; Table S3).

The minimal occurrence of aspartate-derived succinate (m + 2) in untreated 143B cells indicates that the major carbon source for succinate is glutamine through anaplerosis in these cells (Figure 1D; Tables S2 and S3). However, an accumulation of aspartate-derived carbon in succinate (m + 4) was observed in ρ^0 cells or 143B cells treated with antimycin A, but not in untreated 143B cells (Figure 1D; Tables S2 and S3). This indicates that respiration deficiency drives reversed flux through SDH and that the aspartate-derived carbon has therefore entered the mitochondrion (Figure 1E). Like our observations with aspartate labeling, carbon derived from $^{13}C_6$-glucose or $^{13}C_3$-pyruvate was also found as malate (m + 3) and fumarate (m + 3) in untreated 143B cells and

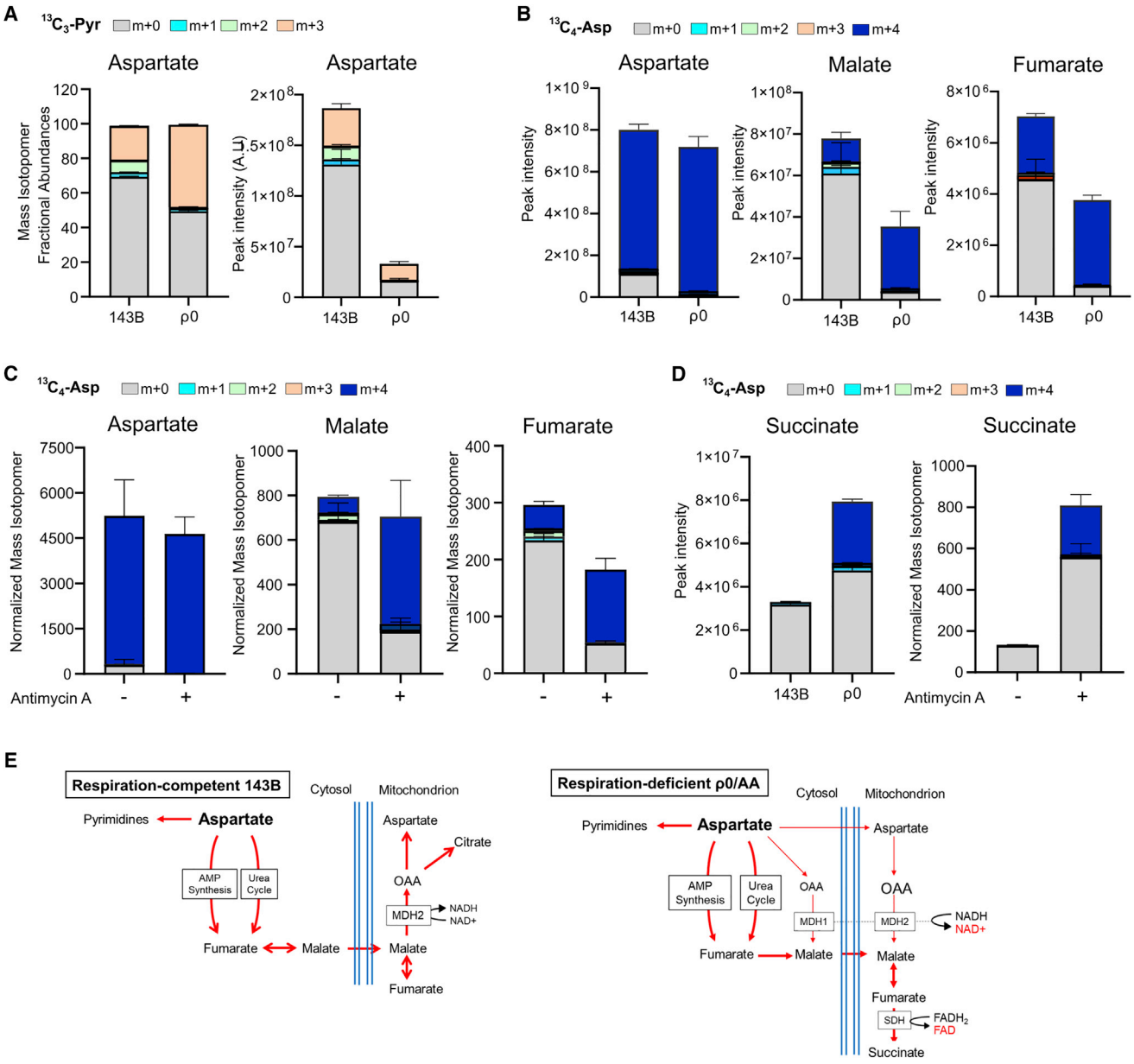

Figure 1. ETC dysfunction drives reductive metabolism to correct mitochondrial redox imbalance

(A) $^{13}C_3$-pyruvate (2 mM) stable isotope tracing (2 h pulse) was used to reveal flux of carbon from pyruvate into aspartate in extracts from 143B and ρ0 cells, as measured by LC-MS. Absolute and relative isotopolog distribution is shown (n = 4).

(B) $^{13}C_4$-aspartate (20 mM) stable isotope tracing (6 h pulse) was used to reveal flux of carbon from aspartate into TCA cycle metabolites in 143B and ρ0 cells, as measured by LC-MS. Absolute isotopolog distribution is shown (n = 4).

(C) $^{13}C_4$-aspartate (20 mM) stable isotope tracing (6 h pulse) consistently showed flux of carbon from aspartate into TCA cycle in cells treated with antimycin A (5 μM), measured by GC-MS. Normalized isotopolog distribution is shown (n = 3).

(D) Isotopolog distribution of succinate from cells treated with $^{13}C_4$-aspartate (20 mM) (12 h pulse) upon respiration deficiency (n ≥ 3).

(E) Schematic summary of aspartate metabolism in respiratory competent (143B) cells and respiratory deficient cells (ρ0/antimycin-A-treated 143B cells). LC-MS quantification exhibits peak intensity, and GC-MS quantification exhibits normalized ion counts. Values in all figure panels denote mean ± SD.

See also Figures S1 and S2 and Tables S1–S8.

was elevated in cells treated with antimycin A (Figures S1A and S1B;Tables S4 and S5). Succinate (m + 3) was only found in ρ^0 cells or cells treated with antimycin A, but not in untreated 143B cells, most likely involving sequential activity of the mitochondrial enzymes pyruvate carboxylase (PC), MDH2, and SDH (Figures S1A and S1B; Tables S1 S4, and S5). To test this possibility, we employed enrichment of the mitochondrial compartment through digitonin permeabilization of cells to obtain

compartment-specific information on the carbon flux (Nonnenmacher et al., 2019; Rinaldi et al., 2021) (Figure S1C). $^{13}C_4$-aspartate labeling demonstrated enrichment of malate (m + 4) and fumarate (m + 4) upon antimycin A treatment and appearance of succinate (m + 4) only with antimycin A (Figure S1D; Table S6). Similarly, $^{13}C_3$-pyruvate labeling showed enrichment of fumarate (m + 3) and appearance of succinate (m + 3) only with antimycin A (Figure S1E; Table S6), suggesting flux through PC, MDH2, and SDH.

Next, we used $^{13}C_5$-glutamine tracing to establish the overall direction of the TCA cycle by assessing the abundance of the (m + 2) and (m + 3) isotopologs of fumarate: these isotopologs indicate the direction of a near-complete turn of the TCA cycle. In the absence of antimycin A, the majority of TCA cycle activity was in the oxidative (m + 2) direction with some flux in the reductive (m + 3) direction (Figure S1F; Table S7). However, upon treatment with antimycin A, only the reductive (m + 3) TCA cycle was observed. Thus, the reductive flux induced by ETC inhibition that we observed from glucose and aspartate was accompanied by a switch of the whole TCA cycle from oxidative to reductive metabolism, as previously described (Mullen et al., 2011).

Aspartate rescues the loss of viability due to inhibition of respiration in multiple cell types (Sullivan et al., 2015), and so we examined whether our reversal of mitochondrial dehydrogenases was similarly conserved. Using $^{13}C_3$-pyruvate labeling, we assessed appearance of succinate (m + 3) to establish the carbon flux in the mitochondrion (since SDH is solely mitochondrial) in other tumor types. In all cell types tested (A549 lung adenocarcinoma, MDA-MB-231 breast carcinoma, HCT116 colon carcinoma, HUH7 hepatoma, and U87 glioblastoma cells), antimycin A caused strong accumulation of succinate (m + 3) and a similar accumulation of absolute succinate levels (Figure S2; Table S8). Thus, reversal of mitochondrial dehydrogenases is a general consequence of inhibition of respiration.

Respiration deficiency drives reversal of MDH2 and SDH

In order to ascertain the exact metabolic pathways through which aspartate could support cell viability, we employed RNA interference (siRNA) and clustered regularly interspaced short palindromic repeats (CRISPR, crRNA) approaches (Figures S3A and S3B). First, we verified that the production of succinate from aspartate was indeed catalyzed by SDH. As expected, both siRNA and crRNA to *SDHB* abrogated the succinate (m + 4) isotopolog derived from $^{13}C_4$-aspartate (Figure 2A; Table S9). Moreover, fumarate accumulation was observed upon SDHB knockdown/deletion in cells treated with antimycin A (Figure S4A; Table S9). We next examined the impact of siRNA to *MDH1* and *MDH2* on the accumulation of intracellular succinate. Knockdown of MDH2 significantly reduced succinate (m + 4) derived from $^{13}C_4$-aspartate, whereas knockdown of MDH1 did not (Figure 2B; Table S10), indicating that aspartate drives reversed flux (compared with their canonical oxidative TCA cycle reaction direction) of both MDH2 and SDH in the mitochondrion (Figure 1E). A similar pattern of malate and succinate labeling was also observed in mitochondrial fractions, confirming that the reversed carbon flux was mitochondrial (Figure S4B; Table S6).

Facilitation of flux through metabolic pathways can arise through removal of terminal reaction products, since this prevents metabolite buildup and product inhibition of enzymatic reactions. In this regard, we hypothesized that succinate should be secreted to avoid product inhibition of the reversed carbon flux through the mitochondrial dehydrogenases. For cells in culture, this would usually be accomplished by export to the medium. Following labeling with $^{13}C_3$-pyruvate for 48 h, we observed accumulation of succinate (m + 3) in the medium of cells treated with antimycin A (Figure 2C). In the same experiment, CRISPR targeting of *MDH2* led to a significant drop in succinate (m + 3), whereas targeting *MDH1* showed no effect (Figure 2C). Analysis of malate (m + 3) in the medium confirmed the flux through MDH2 (Figure 2D). This demonstrates that pyruvate supports reversed flux through MDH2 and SDH and that the malate and succinate thus produced can be exported from the cell, permitting continuous flux through this pathway (Figure 2E). The export of succinate to the medium resulting from this reversed flux was confirmed in multiple cell types, confirming it as a general phenomenon of inhibition of respiration (Figure S4C).

Taken together, these stable isotope tracing and genetic analyses show reversed flux through the mitochondrial dehydrogenases MDH2 and SDH and therefore production of mitochondrial NAD^+ by MDH2.

Mitochondrial NADH oxidation is required for redox rescue of respiration deficiency

Having identified the reversal of MDH2 and consequent mitochondrial NAD^+ production, we aimed to ascertain whether this was essential for viability of respiration-deficient cells. We therefore used CRISPR-based gene deletion to interrogate essential metabolic pathways and assessed cell growth in medium without pyruvate or with addition of pyruvate, aspartate, or α-KB. In the control (tracrRNA:no CRISPR target), antimycin A treatment led to a loss of viability that was rescued by all three metabolites (Figures 3A and S5A; Table S11), as expected. The rescue of viability in each case was accompanied by an increase in the NAD^+/NADH ratio (Figure S5B). Notably, we did not observe any correlation between rescue conditions and reactive oxygen species (ROS) in the mitochondria or cytosol (Figure S5C). In addition, viability rescue upon pyruvate, aspartate, or α-KB was also observed in multiple cell types, confirming that these metabolites are generally essential during respiratory inhibition (Figure S5D; Table S11). Since aspartate is the key determinant of viability in this system (Birsoy et al., 2015; Sullivan et al., 2015), we predicted that it should still rescue viability, irrespective of flux through the mitochondrial dehydrogenases. Similarly, as described above, pyruvate can produce aspartate through PC in a redox-independent fashion and thus, again, would be expected to rescue viability in the absence of the dehydrogenases. Indeed, as expected, targeting MDH1, MDH2, or GOT2 had no effect on viability rescued by pyruvate or aspartate (Figures 3B and 3C; Table S11), even though it reduced flux to succinate from both nutrients (Figures S4B and S5E; Tables S6, S10, and S12). By contrast, the rescue of viability afforded by α-KB was significantly compromised by loss of GOT2 or MDH2 but not MDH1 (Figure 3D; Table S10). These data confirm that either mitochondrial malate or mitochondrial

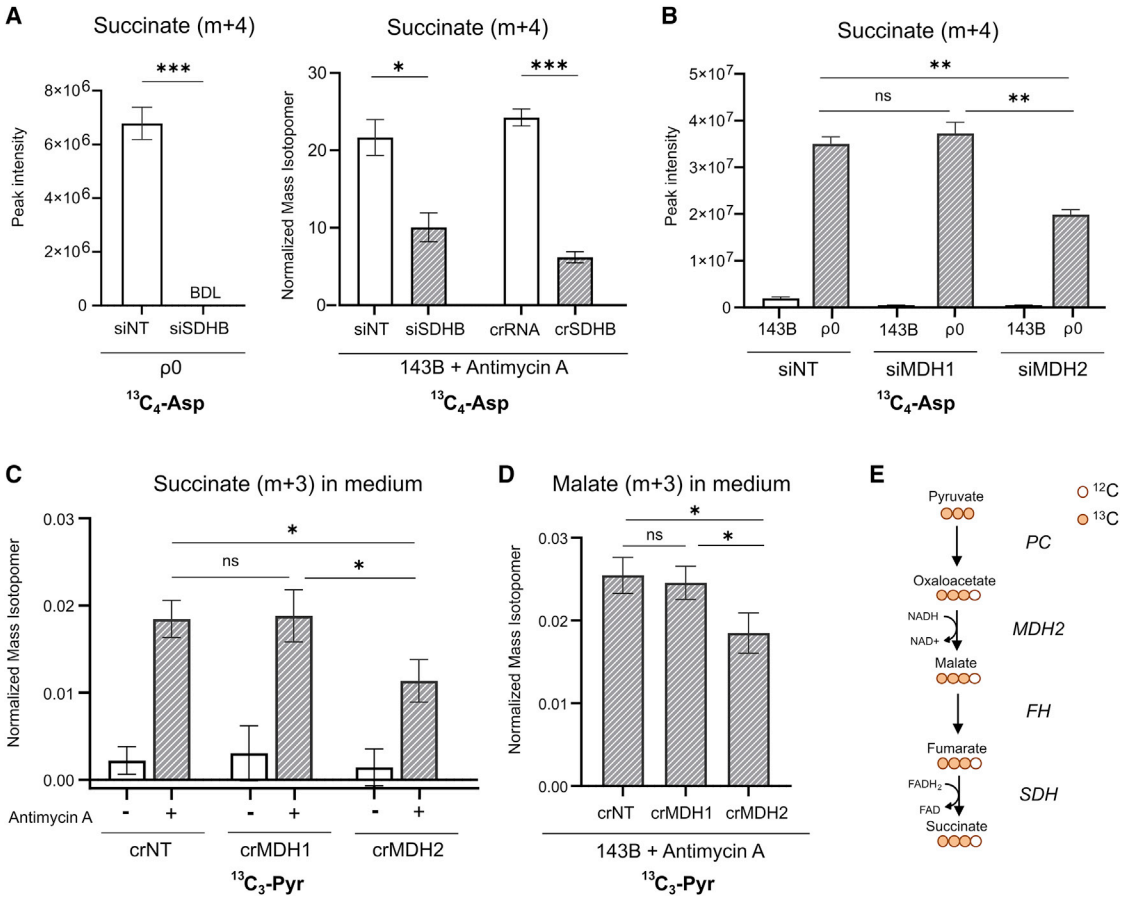

Figure 2. Respiration deficiency drives reversal of mitochondrial dehydrogenases

(A) $^{13}C_4$-aspartate (20 mM) stable isotope tracing (6 h pulse) revealed a significant decrease in the aspartate carbon contribution to succinate upon succinate dehydrogenase (SDHB) inhibition and respiration deficiency (ρ0 cells, LC-MS; antimycin A-treated 143B cells, GC-MS) (n = 3). Unpaired t test, two-tailed.

(B) Significant decrease of carbon contribution from aspartate to succinate was also monitored in ρ0 cells when MDH2—but not MDH1—was inhibited. Absolute isotopolog distribution is shown (LC-MS) (n = 3). One-way ANOVA with Holm-Sidak's multiple comparison test.

(C) $^{13}C_3$-pyruvate (2 mM) stable isotope tracing (48 h) showed accumulation of succinate (m + 3) in the medium exported by 143B cells treated with antimycin A (5 μM) and a significant decrease when MDH2—but not MDH1—was inhibited. Absolute isotopolog distribution is shown (GC-MS) (n = 3). One-way ANOVA with Holm-Sidak's multiple comparison test.

(D) $^{13}C_3$-pyruvate (2 mM) stable isotope tracing (48 h) showed a decrease in pyruvate carbon contribution to malate (m + 3) in the medium upon MDH2 inhibition. Normalized isotopolog distribution is shown (GC-MS) (n = 3). One-way ANOVA with Holm-Sidak's multiple comparison test.

(E) Schematic showing how metabolism of $^3C_3$-pyruvate drives reverse mitochondrial dehydrogenases imbalance in ρ0 cells/143B cells treated with antimycin A.

LC-MS quantification exhibits peak intensity, and GC-MS quantification exhibits normalized ion counts. Values in all figure panels denote mean ± SD. siNT, non-target siRNA; siSHB, SDHB siRNA; siMDH1, MDH1 siRNA; siMDH2, MDH2 siRNA. *$p \leq 0.05$, **$p \leq 0.01$, and ***$p \leq 0.001$, and n.s. indicates the measured values were not statistically different ($p > 0.05$).

See also Figures S3 and S4 and Tables S9 and S10.

oxidation of NADH to NAD^+ is required for the rescue of viability by cytosolic NAD^+ regeneration.

In order to separate the NAD^+/NADH redox status from carbon flux, we made use of doxycycline (DOX)-inducible recombinant cytosolic and mitochondrial NADH oxidases (*Lb*NOXs) that pass electrons from NADH to molecular oxygen, rather than onto carbon-containing substrates (Titov et al., 2016) (Figure S6A). $^{13}C_6$-glucose tracing confirmed that induction of the mitochondrial *Lb*NOX (m*Lb*NOX) restored the TCA cycle to the oxidative direction, since the (m + 2) and (m + 4) isotopologs of succinate appeared, whereas the (m + 3) isotopolog was reduced (Figure S6B; Table S13). However, induction of the cytosolic *Lb*NOX did not restore oxidative TCA cycle activity.

Cells expressing the m*Lb*NOX were able to grow in the absence of pyruvate, aspartate, or α-KB (Figures 3E and S6A; Table S11), indicating that rescue of the mitochondrial NAD^+/NADH ratio is sufficient to confer viability on respiration-deficient cells. Targeting either MDH or GOT2 was well tolerated by these cells when they were treated with antimycin A and deprived of pyruvate (Figure 3E). Cytosolic redox rescue, through expression of *Lb*NOX, rescued viability as expected (Figures 3F and S6A; Table S11), since it substitutes for the redox rescue that would be conferred by pyruvate or α-KB,

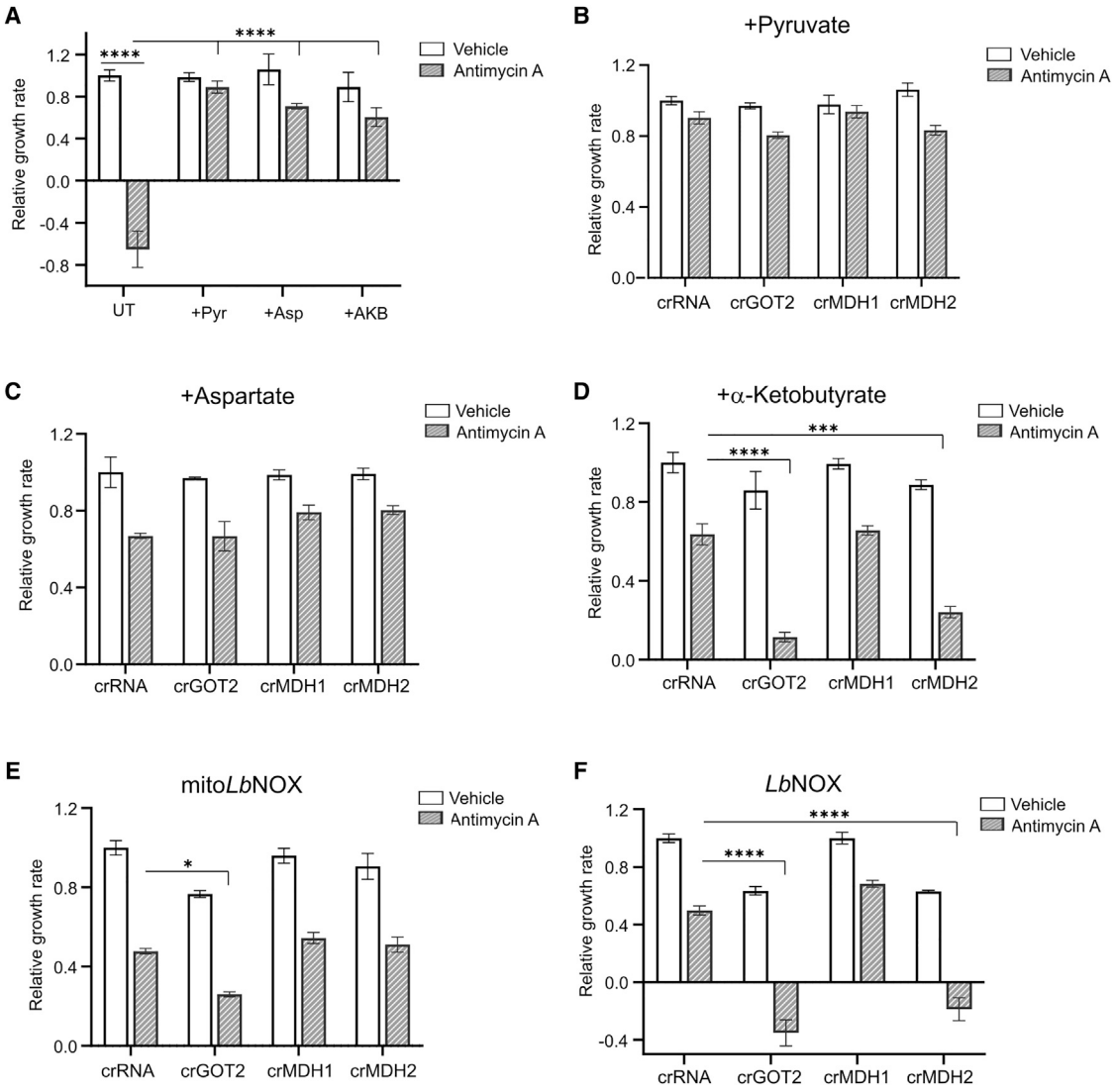

Figure 3. Mitochondrial redox rescue via NADH oxidation is required to sustain viability upon ETC dysfunction

(A–D) (A) The growth rate of 143B cells was determined in media with antimycin A (5 μM) or without (vehicle) in the absence (untreated [UT]) or in the presence of the metabolic rescues pyruvate (Pyr), aspartate (Asp), or α-ketobutyrate (α-KB). In addition, 143B cells were transfected with crGOT2, crMDH1, crMDH2, and crRNA as a control, and growth rate was examined in media with antimycin A (5 μM) or without (vehicle) and supplementation of pyruvate (B), aspartate (C), and α-KB (D).

(E and F) 143B cells expressing the NADH oxidase *Lb*NOX (E) or m*Lb*NOX (F) were transfected with crGOT2, crMDH1, crMDH2, and crRNA as a control, and growth rate was examined in media with antimycin A (5 μM) or without (vehicle).

Cell counts—normalized to cell number at t = 0 when media conditions were applied—were assessed over time and used to calculate growth rate. Values in all figure panels denote mean ± SD (n = 3). For statistical analysis, two-way ANOVA test followed by Tukey's multiple comparison test was performed and statistical significance was calculated, compared with UT + antimycin condition. *$p \leq 0.05$, ***$p \leq 0.001$, and ****$p \leq 0.0001$.

See also Figures S5 and S6 and Tables S10–S14.

acting as electron acceptors for LDH activity. However, as with the rescue of viability by α-KB, targeting MDH2 or GOT2 again led to a loss of viability (Figure 3F). This indicates that oxidation of NADH and consequent redox rebalancing in the cytosol can only restore viability of respiration-deficient cells if the oxidized redox equivalents are transferred into the mitochondrion. This inter-compartmental transfer of NAD^+ equivalents requires the reversal of MDH2.

Mitochondrial NAD^+ generation enables GDH-mediated anaplerosis of the TCA cycle in ETC-deficient cells

To understand how reversal of MDH2 supported viability of ETC-deficient cells, we examined aspects of mitochondrial metabolism that were impacted by conditions of redox rescue. Glutamine is a key anabolic and energetic substrate for many cells but is particularly important in cells with compromised ETC, because it can sustain citrate and fatty acid production through reductive

carboxylation (Metallo et al., 2011; Mullen et al., 2011). Genetic or pharmacological inhibition of complex III activity in cells (that are provided with exogenous pyruvate) leads to accumulation of succinate (Figures 1D and S2; Mullen et al., 2014). This succinate is derived from glutamine, and it accumulates because SDH (complex II) is inactive due to the downstream ETC block in complex III. The accumulation of succinate can therefore act as an indication of anaplerosis of the TCA cycle from glutamine. We examined succinate levels in our cells in the presence of antimycin A and found that in all conditions where viability was rescued, succinate levels accumulated dramatically (Figure 4A; Table S7). Remarkably, however, no accumulation of succinate was observed upon treatment with antimycin A alone (Figure 4A). Utilizing $^{13}C_5$-glutamine tracing (Figure 4B; Table S7), we confirmed that the majority of the succinate in the rescue conditions was indeed derived from glutamine: the majority was labeled (m + 4) and a minority was labeled (m + 3), indicating the expected oxidative and reductive pathways, respectively (Figures 4B–4D and S6C). Importantly, the labeling pattern observed using the recombinant cytosolic *Lb*NOX and mitochondrial m*Lb*NOX was only observed when their expression was induced by DOX, confirming that this rescue is due to NAD^+ regeneration (Figure S6D; Table S7). Again, this facilitation of anaplerotic flux from glutamine was confirmed in other cell types exposed to inhibition of mitochondrial respiration (Figure S6E; Table S14).

Since the accumulation of succinate correlated precisely with the conditions in which mitochondrial redox imbalance was rescued, we reasoned that mitochondrial NAD^+ availability might be limiting for the activity of GDH, a NAD^+-dependent dehydrogenase that converts glutamate to α-ketoglutarate. We therefore examined the transfer of glutamine-derived carbon into glutamate and α-ketoglutarate. The deamidation of glutamine to glutamate can be catalyzed by many enzymes, including amidotransferases that are involved in biosynthetic reactions as well as glutaminases that hydrolyze the amide group. However, none of the glutamine deamidation reactions directly involve redox co-factors, and accordingly, the abundance of the glutamate (m + 5) isotopolog was not significantly affected, neither by antimycin A nor by any of our experimental conditions (Figures 5A and S7A; Table S7). The α-ketoglutarate (m + 5) isotopolog, however, was almost eliminated by the addition of antimycin A (Figure 5B), consistent with the lack of mitochondrial NAD^+ required as a co-factor for GDH. Provision of exogenous pyruvate or α-KB greatly facilitated the production of α-ketoglutarate (m + 5), demonstrating the intercompartmental transfer of NAD^+ equivalents and its facilitation of anaplerosis (Figure 5B; Table S7). Furthermore, the expression of either the cytosolic *Lb*NOX or the mitochondrial m*Lb*NOX facilitated production of α-ketoglutarate (m + 5) (Figures 5B and S7B; Table S7). Incidentally, the overall (m + 0) and (m + 5) levels of α-ketoglutarate were all strongly suppressed upon aspartate supplementation, presumably due to substrate-driven GOT activity promoting consumption of α-ketoglutarate (Figure S7C; Table S7). These data indicate that rescue of redox imbalance, whether mitochondrial (e.g., m*Lb*NOX) or cytosolic (e.g., pyruvate, α-KB, aspartate, and *Lb*NOX), promotes anaplerosis of glutamine-derived carbon in the mitochondrion via GDH. This anaplerotic aspect of redox rescue was conserved in the presence of rotenone, another mitochondrial respiration inhibitor (Figure S7D; Table S15), and across multiple genetically diverse cell lines (Figure S7E; Table S14).

To assess whether the environmental NAD^+/NADH ratio was sufficient to modulate flux through GDH, we performed *in vitro* assays using purified bovine GDH (which is 96% identical to human GDH), glutamate as a substrate, and varying NAD^+ and NADH concentrations—based on previous reports of mitochondrial concentrations and ratios of these co-factors (Anderson et al., 2017; Stein and Imai, 2012). LC-MS analysis revealed a dose-dependent reduction in α-ketoglutarate production as the NAD^+/NADH ratio was reduced (Figure 5C). Thus, we conclude that the mitochondrial NAD^+/NADH ratio controls GDH activity and its anaplerotic capacity.

To assess the importance of GDH-mediated anaplerosis in supporting viability, we inhibited the enzyme using epigallocatechin gallate (EGCG). EGCG treatment prevented both the *Lb*NOX and m*Lb*NOX from rescuing cell viability (Figure 5D; Table S11), indicating that GDH is key for this rescue. Since the redox rescue of viability of ETC-deficient cells requires GDH activity and correlates with entry of carbon into the TCA cycle at α-ketoglutarate, we examined whether supplementation with this metabolite could also rescue viability. Addition of pyruvate or aspartate or α-KB rescued cells from the loss in viability caused by antimycin A treatment, as expected (Figure 5E). Addition of glutamate did not support viability of antimycin A-treated cells, but addition of α-ketoglutarate did rescue viability (Figures 5E and S7F; Table S11), indicating that the key metabolic defect that compromises viability in respiration-deficient cells is the conversion of glutamate to α-ketoglutarate. Taken together, these data indicate that a critical component of the rescue of viability is the transfer of cytosolic oxidative equivalents into the mitochondrion to support GDH activity and cell viability (Figure 5F).

DISCUSSION

Transfer of reductive equivalents from the cytosol into the mitochondrion through the activity of the malate-aspartate shuttle is a well-established paradigm in energy production (Spinelli and Haigis, 2018). Oxidation of NADH by MDH1 in the cytosol allows for continued glycolysis, and the coupled production of NADH by MDH2 in the mitochondrion fuels the ETC and ATP generation by the ATP synthase. A single "cycle" of the malate-aspartate shuttle oxidizes a single NADH molecule in the cytosol and reduces a single NAD^+ molecule in the mitochondrion, and although the carriers of the shuttle are carboxylic and amino acids, there is no net transfer of these. This ensures that under normal circumstances, the shuttle automatically responds solely to equalize NAD^+/NADH ratios between the cytosol and mitochondrion. In theory, the shuttle should run in reverse if there is a buildup of mitochondrial NADH, but the lack of aspartate production that is caused by ETC inhibition disrupts the ability of the shuttle to run. Our observation that pyruvate could rescue viability without a requirement for MDH2 underscores the importance of pyruvate carboxylation as a carbon source for aspartate, as previously reported (Cardaci et al., 2015; Lussey-Lepoutre et al., 2015). However, when we examined "redox" rescues that could not donate carbon (α-KB or expression of *Lb*NOX), we found that their ability to rescue viability was dependent upon GOT2 and MDH2,

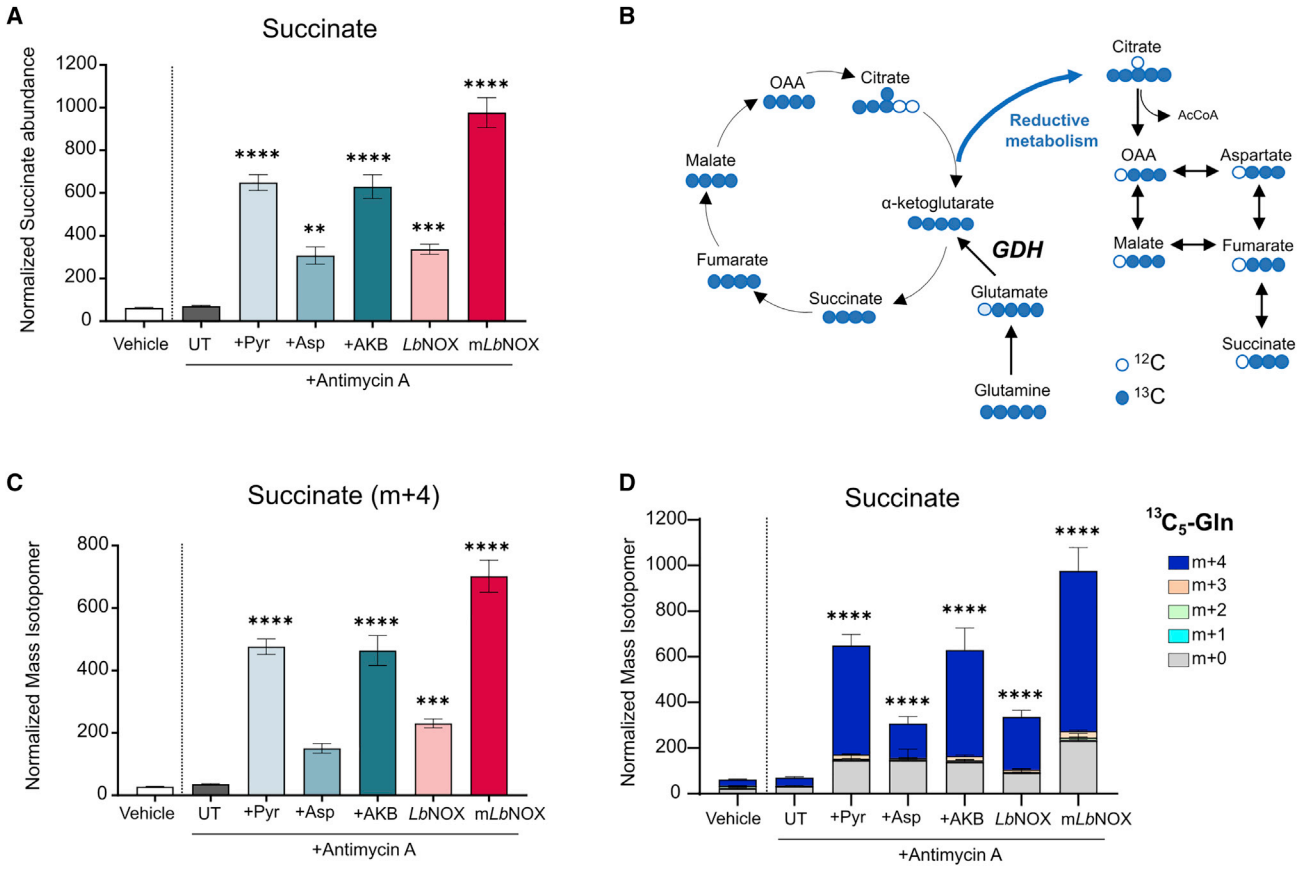

Figure 4. Mitochondrial NAD$^+$ generation sustains viability of ETC-deficient cells by enabling anaplerosis of the TCA cycle

(A) Succinate levels are accumulated in 143B cells when treated with antimycin A (5 μM) in all of the conditions where viability was rescued in the presence of pyruvate (Pyr), aspartate (Asp), α-KB, or expressing *Lb*NOX and m*Lb*NOX. Normalized isotopolog distribution is shown (GC-MS) (n = 4). Statistical significance is calculated, compared with untreated (UT) + antimycin condition.

(B) Schematic showing how $^{13}C_5$-glutamine can be metabolized through a reductive and an oxidative branch of the TCA cycle.

(C and D) $^{13}C_5$-glutamine (4 mM) isotope tracing (6 h pulse) showed a minority of succinate labeled (m + 3), indicating the oxidative and reductive pathways from glutamine (C), and the majority was accumulated in the rescue conditions, deriving from glutamine (m + 4) (D). Normalized isotopolog distribution is shown (GC-MS) (n = 4). Statistical significance is calculated for m + 4 isotopolog, compared with UT + antimycin A condition. GC-MS quantification exhibits normalized ion counts.

Values in all figure panels denote mean ± SD. One-way ANOVA with Dunnett's multiple comparison. **p ≤ 0.01, ***p ≤ 0.001, and ****p ≤ 0.0001.

See also Figures S6 and S7 and Tables S7, S13, and S14.

demonstrating for the first time that reversal of the mitochondrial arm of the shuttle is required.

Here, we provide evidence that the mitochondrial MDH2-mediated oxidation of NADH to NAD$^+$ is coupled to the activity of the GDH and thereby enables anaplerosis from glutamine-derived carbon (Figure 5F). Such coupling of mitochondrial dehydrogenase reactions has previously been reported (Mullen et al., 2014). The mitochondrial α-ketoglutarate thus produced can exit the mitochondrion to drive reductive carboxylation via isocitrate dehydrogenase (IDH) 1, as described in a similar model of ETC deficiency (Gaude et al., 2018), or could be converted into isocitrate via IDH2, with subsequent isomerization to citrate and export from the mitochondrion. Indeed, a dependence upon the mitochondrial citrate carrier SLC25A1 has also been reported in ETC-deficient cells (Birsoy et al., 2015). A further mechanism for supporting viability of respiration-deficient cells through removal of electrons from the ETC via reversal of SDH was recently described (Spinelli et al., 2021).

To drive the mitochondrial arm of the malate-aspartate shuttle in reverse, there must be a source of aspartate. In the case of rescue of viability with exogenous pyruvate, this can come from mitochondrial PC activity (Cardaci et al., 2015; Lussey-Lepoutre et al., 2015), but much of it is derived from glutamine by reductive carboxylation (Sullivan et al., 2015) and is generated by GOT1 in the cytosol (Birsoy et al., 2015). In conditions of redox rescue without carbon (α-KB or expression of *Lb*NOX), only the latter pathway is available and must involve a source of cytosolic oxaloacetate as a substrate for GOT1. Although MDH1 can produce cytosolic oxaloacetate, it would require a source of cytosolic malate to do so. This is unlikely in ETC-deficient cells since cytosolic malate is primarily produced from aspartate via the purine nucleotide and urea cycles, and aspartate itself is limiting in

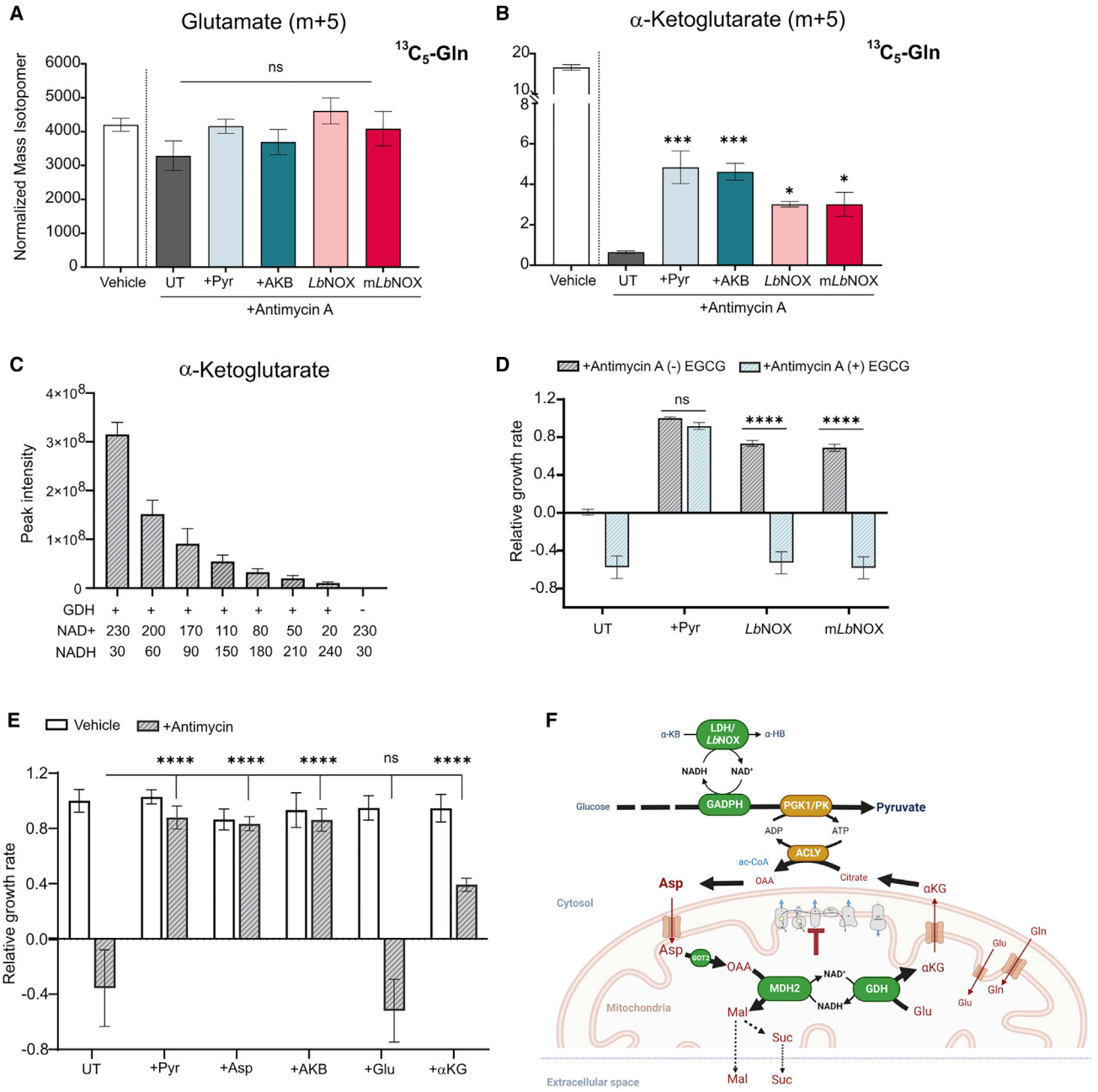

Figure 5. Correction of the mitochondrial redox imbalance by regenerating NAD$^+$ is required for redox rescue of respiration deficiency

(A) $^{13}C_5$-glutamine (4 mM) tracing (6 h pulse) revealed the carbon contribution from glutamine to glutamate (m + 5) was not significantly affected, neither by antimycin A nor by the presence of pyruvate (Pyr), aspartate (Asp), α-KB, and nor by expressing *Lb*NOX and m*Lb*NOX. Normalized isotopolog distribution is shown (GC-MS) (n = 4). Statistical significance is calculated, compared with UT + antimycin A condition. One-way ANOVA with Dunnett's multiple comparison.

(B) $^{13}C_5$-glutamine tracing (6 h pulse) showed a significant reduction of α-ketoglutarate (m + 5) isotopolog by the addition of antimycin A and a rescue in the carbon transfer from glutamine to α-ketoglutarate in the presence of pyruvate (Pyr), α-KB, and expressing *Lb*NOX and m*Lb*NOX. Normalized isotopolog distribution is shown (GC-MS) (n = 4). Statistical significance is calculated, compared with UT + antimycin A condition. One-way ANOVA with Dunnett's multiple comparison.

(C) GDH activity upon NAD$^+$ addition, measured by α-ketoglutarate production using a glutamate-coupled enzyme assay (n = 3). Absolute abundance is shown (LC-MS).

(D and E) The growth rate of 143B cells was determined in media with antimycin A (5 μM), antimycin A + EGCG (50 μM), or without (vehicle), in the absence (UT) or in the presence of the metabolic rescues pyruvate (Pyr), aspartate (Asp), α-KB, glutamate (Glu), or α-ketoglutarate (α-KG) (n ≥ 3). In (D), values represent

(legend continued on next page)

ETC-deficient cells. Indeed, we did not observe a dependence upon MDH1 for the rescue of viability by α-KB or expression of *Lb*NOX. The other possible source of cytosolic oxaloacetate is from the activity of ATP citrate lyase (ACLY) during reductive carboxylation. Although there is no cytosolic NAD^+-consuming dehydrogenase in this pathway whose activity could be stimulated by LDH or *Lb*NOX activity, the reversal of ACLY itself requires an input of ATP. It is therefore possible that there is an energetic coupling based upon redox-dependent stimulation of glycolytic ATP production (as shown in Figure 5F) and consequent stimulation of ACLY activity.

Our data, combined with those from other groups, demonstrate the remarkable plasticity of cellular metabolism, and here, we provide new insight into metabolic communication between the cytosolic and mitochondrial compartments. The fact that cytosolic redox rescue can act as a "rheostat" to promote anaplerosis of mitochondrial metabolites underscores this close mutual metabolic dependency between the mitochondrion and the cytosol. Perturbations of cellular metabolism, whether disease- or therapy-induced, can elicit metabolic pathway dependencies that can be targeted in therapeutic approaches based upon synthetic lethality (Gui et al., 2016; Zecchini and Frezza, 2017). Our data suggest that the therapeutic value of targeting respiration could be enhanced by targeting one or more of the metabolic enzymes that promote generation of aspartate from glutamine via reductive carboxylation. Inhibition of GDH or ACLY might exert unwanted side effects, due to the pivotal and nodal nature of these enzymes in cellular metabolism. However, as a rheostatic controller for GDH and anaplerosis, MDH2 might represent a better complement to inhibition of respiration for cancer therapy.

Limitations of the study

Here, we demonstrate that respiration-deficient cells are restricted in anaplerosis of the TCA cycle due to redox inhibition of GDH. Furthermore, we show that cytosolic redox rescue leads to reversal of MDH2 and consequent rescue of anaplerosis via GDH activity. However, when this mechanism occurs *in vivo* remains to be deciphered. Going forward, it will be important to ascertain this and to understand whether the suggested synthetic lethality between ETC inhibition and MDH2 inhibition is therapeutically exploitable *in vivo*.

STAR★METHODS

Detailed methods are provided in the online version of this paper and include the following:

- KEY RESOURCES TABLE
- RESOURCE AVAILABILITY
  - Lead contact
  - Materials availability
  - Data and code availability
- EXPERIMENTAL MODEL AND SUBJECT DETAILS
  - Cell culture and treatments
- METHOD DETAILS
  - Cas9 induction and cell transfection
  - RNAi transfection
  - Generation of inducible *Lb*NOX and m*Lb*NOX stable cells by lentiviral infection
  - Growth rate
  - IncuCyte cell proliferation assay
  - Isotope labeling and metabolite extraction
  - Liquid chromatography–mass spectrometry (LC-MS) analysis
  - Gas chromatography–mass spectrometry (GC-MS) analysis
  - Compartment specific-metabolic measurements
  - Glutamate dehydrogenase activity assay
  - Measurement of NAD^+/NADH
  - Measurement of reactive oxygen species (ROS)
  - RNA extraction, cDNA synthesis and quantitative PCR
  - Western Blot
- QUANTIFICATION AND STATISTICAL ANALYSIS

SUPPLEMENTAL INFORMATION

Supplemental information can be found online at https://doi.org/10.1016/j.molcel.2022.10.005.

ACKNOWLEDGMENTS

P.A.-M was supported by a Marie Skłodowska-Curie Actions individual fellowship and the Beug Foundation. A.V. was supported by Fonds Wetenschappelijk Onderzoek (FWO Vlaanderen). J.E.-H. was supported by an MRC studentship. J.C.A was supported by a Cancer Research UK Career Development Fellowship (C47559/A16243). S.-M.F. acknowledges funding from the European Research Council under the ERC Consolidator grant agreement no. 771486–MetaRegulation, FWO Projects, Fonds Baillet Latour, KU Leuven-FTBO/Internal Funding, Stichting Tegen Kanker and the King Baudouin Foundation. Work in the A.J.F. group was supported by a Wellcome Trust-ISSF grant, funding from Barts Charity (MGU0404), and by a Cancer Research UK Centre Grant to Barts Cancer Institute (C355/A25137). The illustrations in the graphical abstract and Figure 5F were created using BioRender.com.

AUTHOR CONTRIBUTIONS

Conceptualization, P.A.-M., M.M.-H., and A.J.F.; methodology, P.A.-M., J.E.-H., and A.J.F.; software: J.W.; formal analysis, P.A.-M., J.E.-H., and A.J.F.; investigation, P.A.-M., A.V., J.E.-H., M.R., E.A., X.L., A.N.G., D.B., J.W., J.M.J., and A.P.; resources, J.C.A., R.M.S.-M., S.-M.F., M.M.-H., and A.J.F.; writing – original draft, A.J.F.; writing – review & editing, P.A.-M., J.E.-H., S.-M.F., M.M.-H., and A.J.F.; funding acquisition, R.M.S.-M., S.-M.F., M.M.-H., and A.J.F.

DECLARATION OF INTERESTS

S.-M.F. has received funding from Alesta Therapeutics, Bayer AG, Merck, and Black Belt Therapeutics; has consulted for Fund+; and serves on the advisory board of Alesta Therapeutics and *Molecular Cell*.

mean ± SEM. In (E), statistical significance is represented, compared with UT + antimycin A condition. Two-way ANOVA with a Tukey's multiple comparison test was performed.

(F) Schematic showing how cytosolic regeneration of NAD^+ can restore mitochondrial redox imbalance through reversal of MDH2 in respiration-deficient cells. Values denote mean ± SD. *$p \leq 0.05$, ***$p \leq 0.001$, and ****$p \leq 0.0001$, and n.s. indicates the measured values were not statistically different ($p > 0.05$). See also Figure S7 and Tables S7 and S11.

INCLUSION AND DIVERSITY

We support inclusive, diverse, and equitable conduct of research.

Received: October 14, 2021
Revised: June 13, 2022
Accepted: October 3, 2022
Published: November 2, 2022

REFERENCES

Anderson, K.A., Madsen, A.S., Olsen, C.A., and Hirschey, M.D. (2017). Metabolic control by sirtuins and other enzymes that sense NAD^+, NADH, or their ratio. Biochim. Biophys. Acta Bioenerg. *1858*, 991–998.

Birsoy, K., Wang, T., Chen, W.W., Freinkman, E., Abu-Remaileh, M., and Sabatini, D.M. (2015). An essential role of the mitochondrial electron transport chain in cell proliferation is to enable aspartate synthesis. Cell *162*, 540–551.

Cardaci, S., Zheng, L., Mackay, G., Van Den Broek, N.J.F., Mackenzie, E.D., Nixon, C., Stevenson, D., Tumanov, S., Bulusu, V., Kamphorst, J.J., et al. (2015). Pyruvate carboxylation enables growth of SDH-deficient cells by supporting aspartate biosynthesis. Nat. Cell Biol. *17*, 1317–1326.

Decensi, A., Puntoni, M., Goodwin, P., Cazzaniga, M., Gennari, A., Bonanni, B., and Gandini, S. (2010). Metformin and cancer risk in diabetic patients: a systematic review and meta-analysis. Cancer Prev. Res. (Phila) *3*, 1451–1461.

El-Mir, M.Y., Nogueira, V., Fontaine, E., Avéret, N., Rigoulet, M., and Leverve, X. (2000). Dimethylbiguanide inhibits cell respiration via an indirect effect targeted on the respiratory chain complex I. J. Biol. Chem. *275*, 223–228.

Fernandez, C.A., Des Rosiers, C., Previs, S.F., David, F., and Brunengraber, H. (1996). Correction of 13C mass isotopomer distributions for natural stable isotope abundance. J. Mass Spectrom. *31*, 255–262.

Gaude, E., Schmidt, C., Gammage, P.A., Dugourd, A., Blacker, T., Chew, S.P., Saez-Rodriguez, J., O'Neill, J.S., Szabadkai, G., Minczuk, M., and Frezza, C. (2018). NADH shuttling couples cytosolic reductive carboxylation of glutamine with glycolysis in cells with mitochondrial dysfunction. Mol. Cell *69*. 581.e7–593.e7.

Gui, D.Y., Sullivan, L.B., Luengo, A., Hosios, A.M., Bush, L.N., Gitego, N., Davidson, S.M., Freinkman, E., Thomas, C.J., and Vander Heiden, M.G. (2016). Environment dictates dependence on mitochondrial complex I for NAD^+ and aspartate production and determines cancer cell sensitivity to metformin. Cell Metab. *24*, 716–727.

King, M.P., and Attardi, G. (1989). Human cells lacking mtDNA: repopulation with exogenous mitochondria by complementation. Science *246*, 500–503.

Livak, K.J., and Schmittgen, T.D. (2001). Analysis of relative gene expression data using real-time quantitative PCR and the $2^{-\Delta\Delta C}{}_T$ method. Methods *25*, 402–408.

Lorendeau, D., Rinaldi, G., Boon, R., Spincemaille, P., Metzger, K., Jäger, C., Christen, S., Dong, X., Kuenen, S., Voordeckers, K., et al. (2017). Dual loss of succinate dehydrogenase (SDH) and complex I activity is necessary to recapitulate the metabolic phenotype of SDH mutant tumors. Metab. Eng. *43*, 187–197.

Lussey-Lepoutre, C., Hollinshead, K.E., Ludwig, C., Menara, M., Morin, A., Castro-Vega, L.J., Parker, S.J., Janin, M., Martinelli, C., Ottolenghi, C., et al. (2015). Loss of succinate dehydrogenase activity results in dependency on pyruvate carboxylation for cellular anabolism. Nat. Commun. *6*, 8784.

Metallo, C.M., Gameiro, P.A., Bell, E.L., Mattaini, K.R., Yang, J., Hiller, K., Jewell, C.M., Johnson, Z.R., Irvine, D.J., Guarente, L., et al. (2011). Reductive glutamine metabolism by IDH1 mediates lipogenesis under hypoxia. Nature *481*, 380–384.

Mullen, A.R., Hu, Z., Shi, X., Jiang, L., Boroughs, L.K., Kovacs, Z., Boriack, R., Rakheja, D., Sullivan, L.B., Linehan, W.M., et al. (2014). Oxidation of alpha-ketoglutarate is required for reductive carboxylation in cancer cells with mitochondrial defects. Cell Rep. *7*, 1679–1690.

Mullen, A.R., Wheaton, W.W., Jin, E.S., Chen, P.-H., Sullivan, L.B., Cheng, T., Yang, Y., Linehan, W.M., Chandel, N.S., and DeBerardinis, R.J. (2011). Reductive carboxylation supports growth in tumour cells with defective mitochondria. Nature *481*, 385–388.

Nonnenmacher, Y., Palorini, R., and Hiller, K. (2019). Determining compartment-specific metabolic fluxes. Methods Mol. Biol. *1862*, 137–149.

Owen, M.R., Doran, E., and Halestrap, A.P. (2000). Evidence that metformin exerts its anti-diabetic effects through inhibition of complex 1 of the mitochondrial respiratory chain. Biochem. J. *348*, 607–614.

Rinaldi, G., Pranzini, E., Van Elsen, J., Broekaert, D., Funk, C.M., Planque, M., Doglioni, G., Altea-Manzano, P., Rossi, M., Geldhof, V., et al. (2021). In vivo evidence for serine biosynthesis-defined sensitivity of lung metastasis, but not of primary breast tumors, to mTORC1 inhibition. Mol. Cell *81*. 386.e7–397.e7.

Spinelli, J.B., and Haigis, M.C. (2018). The multifaceted contributions of mitochondria to cellular metabolism. Nat. Cell Biol. *20*, 745–754.

Spinelli, J.B., Rosen, P.C., Sprenger, H.G., Puszynska, A.M., Mann, J.L., Roessler, J.M., Cangelosi, A.L., Henne, A., Condon, K.J., Zhang, T., et al. (2021). Fumarate is a terminal electron acceptor in the mammalian electron transport chain. Science *374*, 1227–1237.

Stein, L.R., and Imai, S. (2012). The dynamic regulation of NAD metabolism in mitochondria. Trends Endocrinol. Metab. *23*, 420–428.

Sullivan, L.B., Gui, D.Y., Hosios, A.M., Bush, L.N., Freinkman, E., and Vander Heiden, M.G. (2015). Supporting aspartate biosynthesis is an essential function of respiration in proliferating cells. Cell *162*, 552–563.

Titov, D.V., Cracan, V., Goodman, R.P., Peng, J., Grabarek, Z., and Mootha, V.K. (2016). Complementation of mitochondrial electron transport chain by manipulation of the NAD^+/NADH ratio. Science *352*, 231–235.

Wheaton, W.W., Weinberg, S.E., Hamanaka, R.B., Soberanes, S., Sullivan, L.B., Anso, E., Glasauer, A., Dufour, E., Mutlu, G.M., Budigner, G.S., and Chandel, N.S. (2014). Metformin inhibits mitochondrial complex I of cancer cells to reduce tumorigenesis. eLife *3*. e02242.

Wills, J., Edwards-Hicks, J., and Finch, A.J. (2017). AssayR: a simple mass spectrometry software tool for targeted metabolic and stable isotope tracer analyses. Anal. Chem. *89*, 9616–9619.

Zecchini, V., and Frezza, C. (2017). Metabolic synthetic lethality in cancer therapy. Biochim. Biophys. Acta Bioenerg. *1858*, 723–731.

STAR★METHODS

KEY RESOURCES TABLE

REAGENT or RESOURCE	SOURCE	IDENTIFIER
Antibodies		
PHGDH	Merck Sigma	HPA021241; RRID:AB_1855299
Tom20	Cell Signaling Technology	42406S
Cytochrome c	BD Pharmigen	556433; RRID:AB_396417
GOT2	Bethyl laboratories	A304-356A-T
MDH1	Bioss Inc	BS-3996R; RRID:AB_10855508
MDH2	NEB	11908S
Tubulin	Cell Signaling Technology	2144S; RRID:AB_2210548
RPL28	Proteintech	16649-1-AP; RRID:AB_2254021
FLAG M2	Merck Sigma	F1804
Vinculin	Cell Signaling Technology	4650; RRID:AB_10559207
VDAC1	Santa Cruz technology	SC-390996; RRID:AB_2750920
HRP-linked secondary antibody anti rabbit	Cell Signaling Technology	7074
HRP-linked secondary antibody anti mouse	Cell Signaling Technology	7076
Chemicals, peptides, and recombinant proteins		
Uridine	Merck Sigma	U3003
Antimycin	Merck Sigma	A8674
Rotenone	Merck Sigma	R8875
Epigallocatechin gallate (EGCG)	Merck Sigma	E4143
Sodium pyruvate	Merck Sigma	P8574
a-Ketobutyric acid (AKB)	Merck Sigma	K401
L-Aspartic acid	Merck Sigma	A7219
Glutaric acid	Merck Sigma	G3407
Dimethyl α-oxoglutarate (aKG)	Merck sigma	349631
Blasticidin	Invitrogen	A1113903
Lipofectamine RNAiMAx	Life Technologies	13778075
Lipofectamine 2000	ThermoFisher Scientific	11668030
Geneticin	Life Technologies	10131-035
Puromycin dihydrochloride	Life technologies	A1113803
Doxycycline hyclate	Merck Sigma	A9891
D-Glucose	Merck Sigma	G7021
L-Glutamine	Merck Sigma	G3126
DMSO	Merck Sigma	D4540
Ammonium carbonate	Fisher Scientific	10785511
Methoxyamine	Merck Sigma	226904
Pyridine	Merck Sigma	270970
N-(tert-butyldimethylsilyl)-N-methyl-trifluoroacetamide	Merck Sigma	375934
Tert-butyldimethylchlorosilane (TBDMS)	Merck Sigma	375934
Methanol	Fisher Scientific	10031094
LC-MS proof H20	Fisher Scientific	10505904
Acetonitrile	Fisher Scientific	10001334
Chloroform	Fisher Scientific	10607602
Digitonin	Merck Sigma	D141
Sucrose	Merck Sigma	S9378

(*Continued on next page*)

Continued

REAGENT or RESOURCE	SOURCE	IDENTIFIER
Mannitol	Merck Sigma	M4125
KH2PO4	Merck Sigma	P5655
MgCl2	Merck Sigma	M8266
HEPES	Merck Sigma	H4034
EGTA	Merck Sigma	E3889
Fatty acid-free BSA	Merck Sigma	10775835001
Bovine glutamate dehydrogenase	Merck Sigma	G2626
Glutamate	Merck Sigma	G1626
ADP	Merck Sigma	A5285
NADH	Merck Sigma	N8129
NAD^+	Merck Sigma	N0632
Dodecyltrimethylammonium bromide	Merck Sigma	A553
NaOH	Merck Sigma	S5881
HCl	Merck Sigma	320331
Tris base	Merck Sigma	T6066
RIPA buffer	Thermo Scientific	89901
Protease inhibitor	Merck Sigma	5892970001
Phosphatase inhibitor	Merck Sigma	4906845001
Laemmli buffer	Bio-RAD	1610747
Tween-20	Merck Sigma	P9416
Chloromethyl-2',7'-dichlorodihydrofluorescein diacetate acetyl ester (CM-H2DCFDA)	Invitrogen	C6827
MitoSox Red	Invitrogen	M36008
D-Glucose 13C6	Merck Sigma	389374
L-Aspartic acid-13C4	Merck Sigma	604852
L-Glutamine-13C5	Merck Sigma	605166
Sodium pyruvate 13C3	Merck Sigma	490717
Critical commercial assays		
SuperSignal West Pico PLUS Chemiluminescent Substrate	ThermoFisher Scientific	34579
Pierce BCA Protein Assay Kit	ThermoFisher Scientific	23225
Precast gel NuPAGE Novex 4-12% Bis-Tris	Thermo Scientific	NP0336BOX
iBlot transfer stacks	ThermoFisher Scientific	IB301002
NAD^+ NADH Glo Assay kit	Promega	G9071
miRNeasy extraction kit	Qiagen	217084
Transcriptor First Strand cDNA synthesis kit	Roche	04379012001
KAPA SYBR FAST qPCR Kit	Roche Diagnostics	07959389001
Experimental models: Cell lines		
A549	ATCC	CCL-185
143B	ATCC	CRL-8303
MDA-MB-231	ATCC	HTB-26
HCT116	ATCC	CCL-247
HUH7	JCRB cell bank	JCRB0403
U87	ATCC	HTB-14
ρ0206 (p0)	Laboratory of Giuseppe Attardi	NA
HEK293T	ATCC	CRL-3216

(*Continued on next page*)

Continued

REAGENT or RESOURCE	SOURCE	IDENTIFIER
Oligonucleotides		
Edit-R tracrRNA	Dharmacon	U-002005-XX
crRNA GOT2 (1)	Dharmacon	011674-01-0002
crRNA GOT2 (2)	Dharmacon	011674-02-0002
crRNA MDH1 (1)	Dharmacon	009264-01-0002
crRNA MDH1 (2)	Dharmacon	009264-02-0002
crRNA MDH2 (1)	Dharmacon	0084394-01-0002
crRNA MDH2 (2)	Dharmacon	0084394-02-0002
crRNA SDHB (1)	Dharmacon	011773-01-0002
crRNA SDHB (2)	Dharmacon	011773-02-0002
ON-TARGETplus SMARTpool siRNA against SDHB	Dharmacon	L-011773-02-008
ON-TARGETplus SMARTpool siRNA non targeting control	Dharmacon	D-001810-10-05
Recombinant DNA		
LentiCas9-Blast	Addgene	52962
LbNOX	Addgene	75285
mitoLbNOX	Addgene	74448
pLVX-TRE3G	Takara-Clontech	631187
PsPAX	Addgene	12260
pMD2.G	Addgene	12259
pLVX-TRE3G-Luc	Takara-Clontech	631354
Software and algorithms		
MATLAB	NA	NA
Xcalibur	Agilent	NA
AssayR	Elixer	NA
IncuCyte ZOOM 2016B	ESSEN Bioscience	NA
Prism 9.1.0	GraphPad	NA
FlowJo v10	BD Bioscience	NA
Other		
Dulbecco's Modified Eagle's Medium	ThermoFisher Scientific	11965084
Fetal bovine serum	Life Technologies	F7524
Pencillin/streptomycin	ThermoFisher Scientific	15140122
Opti-MEM	ThermoFisher Scientific	31985062

RESOURCE AVAILABILITY

Lead contact

Further requests for resources should be directed to the lead contact, Andrew Finch (a.finch@qmul.ac.uk).

Materials availability

This study did not generate new unique reagents, except of genetically manipulated cell lines based on commercially available constructs.

Data and code availability

- The published article includes all analysed data in supplementary tables. The mass spectrometry files supporting the current study are available upon reasonable request from the lead contact. Imaging data are available from Mendeley Data V1 using the https://doi.org/10.17632/8gczwsy26v.1.
- This paper does not report original code.
- Any additional information required to reanalyse the data reported in this paper is available from the lead contact upon request.

EXPERIMENTAL MODEL AND SUBJECT DETAILS

Cell culture and treatments

Osteosarcoma 143B, lung adenocarcinoma A549, breast carcinoma MDA-MB-231, colon carcinoma HCT116, hepatoma HUH7 and glioblastoma U87 cell lines were cultured in Dulbecco's Modified Eagle's Medium (DMEM) (ThermoFisher) supplemented with 10% heat-inactivated fetal bovine serum (Life Technologies) and 1% penicillin/streptomycin. The heat-inactivation of the fetal bovine serum was performed at 55°C for 45 minutes. ρ0206 (ρ0 cells) were also supplemented with 50 μg/ml of uridine, unless otherwise specified. The concentrations of compounds (Sigma) used in different treatments were 5 μM (143B and U87), 2.5 μM (HCT116), 2 μM (HUH7), 1 μM (A549 and MDA-MB-231) antimycin A (AA), 1 μM Rotenone (Rot), 50 μM Epigallocatechin gallate (EGCG), 2 mM Sodium Pyruvate (Pyr), 2 mM α-Ketobutyric acid (AKB), 20 mM L-Aspartatic acid (Asp), 4 mM Glutaric acid (Glu), and 4 mM Dimethyl 2-oxoglutarate (aKG). All cells were maintained at 37°C and 5% CO_2 and 95% relative humidity. All cell lines were regularly tested negative for mycoplasma infection.

METHOD DETAILS

Cas9 induction and cell transfection

143B cells constitutively expressing Cas9 nuclease were generated by transducing lentiCas9-Blast lentivirus (gift from Feng Zhang, Addgene Plasmid #52962). Transduced cells were selected with 6 μg/mL blasticidin. 143B-Cas9 cells were seeded in a 12-well plate at 1.5×10^5 cells per well one day prior to transfection. Two different Edit-R synthetic crRNAs per gene (Dharmacon) and tracrRNA (Dharmacon) were individually resuspended in 10 mM Tris-HCl pH7.5 to a concentration of 100 μM. crRNA and tracrRNA were combined at equimolar ratio and a final concentration of 100 nM crRNA:tracrRNA complex was used for transfection. Cells were transfected using 4 μL/well of Lipofectamine RNAiMax (Life Technologies, 13778075). After 6 h, transfection media was removed and cells were washed once, and subsequently cultured in complete DMEM containing 2 mM Pyruvate. The next days, cells were counted and plated for the subsequent experiment. The targeting sequences used are: GOT2 (#011674-01-0002, *GTGCGCCACTTCATCGAACA* and #011674-02-0002 *GCGTGTAGGAGCCTTCACTA*), MDH1 (#009264-01-0002, *ACCTTACCTTGATTACAACA* and #009264-02-0002 *ATTACCCACAACAATAACCT*), MDH2 (#0084394-01-0002, *GGATGATGGTCTTCCCAGCA* and #0084394-02-0002 *TCCATT CATTGCATCCACAA*), SDHB (#011773-01-0002, *GATTGACACCAACCTCAATA* and #011773-02-0002 *GTCTGGGTCCCATCGA TAGA*).

RNAi transfection

Cells were plated at a concentration of 1.5×10^5 cells per well into 12-well dishes tissue culture plates in standard culture conditions for 24 hours. Cells were then transfected with siRNA for a final concentration of 100 nM using RNAiMax transfection reagent (Life Technologies, 13778075) according to the manufacturer's protocol. siRNA constructs were obtained from a predesigned pool siRNAs targeting SDHB (ON-TARGETplus SMART, # L-011773-02-008 Dharmacon) and non-targeting control (Scramble siRNA #D-001810-10-05 Dharmacon) were included as negative control. Six hours post transfection, cells were counted and plated for subsequent assays, which were performed 48 h after transfection. Efficiency of gene knockdown was evaluated by qRT-PCR.

Generation of inducible *Lb*NOX and m*Lb*NOX stable cells by lentiviral infection

In order to express genetically encoded tools for manipulation of NAD^+/NADH, *Lb*NOX (gift from Vamsi Mootha, Addgene plasmid #75285) and m*Lb*NOX (gift from Vamsi Mootha, Addgene plasmid #74448) were cloned into Tet-On 3G inducible expression lentiviral system pLVX-TRE3G (Takara-Clontech, 631187). Lentiviral particles containing inducible vectors were produced using HEK293T cells. $6x10^6$ cells were seeded per 10cm dish (one plate per lentivirus) in 10 mL of DMEM (ThermoFisher) +10% Fetal Bovine Serum (FBS). The next evening the medium was replaced with Opti-MEM (Thermo Fisher) and cells were transfected with 33 μl Lipofectamine 2000 (ThermoFisher, 11668030), 3.5 μg psPAX2 (Addgene plasmid #12260), 1.5 μg pMD2.G (Addgene plasmid #12259) and 6 μg of the pLVX-TRE3G vector of interest (including pLVX-TRE3G-Luc control vector, expressing Luciferase, obtained from Clontech). Two days after transfection, medium was collected, filtered, and stored at -80C. 143B Tet3G cells were produced first using lentivirus from pLVX-Tet3G (Clontech) vector and then 143B Tet3G cells were infected with 500 uL of the corresponding lentivirus from pLVX-TRE3G-Luciferase, *Lb*NOX or m*Lb*NOX, to generate corresponding cell lines. 24h post infection medium was replaced. After an additional 24h, cells were selected with 400 μg/mL geneticin (Life Technologies, 10131-035) ± 2 μg/mL puromycin (Life Technologies, A1113803). Expression of *Lb*NOX and m*Lb*NOX in stable cells was induced by adding doxycycline (0.5 μg/mL) and validated by western blot.

Growth rate

For growth experiments, cells were plated into replicate 24-well dishes (Corning), with initial seeding density of 15,000 (143B), 20,000 (A549), 30,000 (U87 and HCT116), and 40,000 (MDA-MB-231 and HUH7) cells per well (initial count). Treatments were directly added and carried out for 72h, during which cells were grown in a humidified environment at 37 °C with 5% CO2. After 72h, cells were trypsinized and counted (final count) using a Countess™ II Automated Cell Counter (Thermo Fisher Scientific, MA, USA). Cell number

change was calculated by subtracting the initial count from the final count, and the growth rate was determined using the following formula. Growth rate was subsequently normalized to control condition, unless stated otherwise.

$$\text{Growth rate } [1/h] = \frac{LN(\text{cell number } T1) - LN(\text{cell number } T0)}{time(T1) - time(T0)}$$

Cell number and growth rate calculation are detailed in Table S11.

IncuCyte cell proliferation assay

143B cells were seeded in 100 ul of DMEM at 2500 cells/well in a 96-well plate. After 8h, 100 ul of media containing 2x concentration of each treatment was added per well. The plate was then placed in the IncuCyte ZOOM™ system (ESSEN BioScience). Live-cell images were obtained every 4 h during 72 h using a 10× objective lens (four images per well) within the instrument, and cell density was analyzed using Classic Confluence Analysis with IncuCyte ZOOM 2016B software.

Isotope labeling and metabolite extraction

Cells were pulsed with heavy isotopes (Isotec, Sigma) dissolved in DMEM (A14430 from ThermoFisher) to concentrations of 25 mM glucose (389374 Merck Sigma) (1h pulse), 4 mM glutamine (605166 Merck Sigma) (6h pulse), 2 mM pyruvate (490717 Merck Sigma) (6h pulse) or 20 mM aspartate (604852 Merck Sigma) (12h pulse). Metabolite extractions were performed using the methods previously described (Lorendeau et al., 2017). Briefly, individual wells of a 6-well plate were washed with ice-cold blood bank saline then extracted in 0.5ml extraction buffer (50% methanol, 30% acetonitrile, 20% water at -20 °C or lower). Extracts were centrifuged at maximum speed and stored at -80 °C. For GC-MS measurements, 250 μL –20°C cold chloroform was added, and samples were vortexed at 4 °C for 10 min. Phase separation was achieved by centrifugation at 4 °C for 10 min, after which the methanol phase (containing the total polar metabolites content) was separated and dried by vacuum centrifugation. To analyse metabolite abundances in media samples, cells were cultured with media containing isotope labelling for 48 h. After, supernantant was collected and immediately frozen in dry ice. 200 μL of this supernatant was extracted as already described. Metabolite abundances and ^{13}C labelling patterns were analysed by either gas or liquid chromatography–mass spectrometry.

Liquid chromatography–mass spectrometry (LC-MS) analysis

LC-MS was carried out using a Thermo Ultimate 3000 HPLC inline with a Q Exactive mass spectrometer. A 32 min gradient was developed over a 100 mm x 4.6 mm ZIC-pHILIC column with a guard column (Merck-Millipore) from 10% buffer A (20 mM ammonium carbonate), 90% buffer B (acetonitrile) to 95% buffer A, 5% buffer B. Samples were acquired in positive-negative switching mode and standard ESI source and spectrometer settings were applied (typical scan range 75-1050 Da). Metabolites were identified by standard metabolite matching to m/z and retention time. Integrated peak areas and label incorporation were quantified using AssayR (Wills et al., 2017). Overlapping citrate and isocitrate peaks were analysed as a single (iso)citrate peak. Peak intensity was obtained by integrating peak area using XCalibur.

Gas chromatography–mass spectrometry (GC-MS) analysis

The samples were derivatized and measured as previously described (Lorendeau et al., 2017). Briefly, polar metabolites were derivatized in 20 μL of 20 mg/ml methoxyamine in pyridine per sample for 90 min at 37 °C. Subsequently, 15 μL of N-(tert-butyldimethylsilyl)-N-methyl-trifluoroacetamide, with 1 % tert-butyldimethylchlorosilane were added to 7.5 μL of each derivative and incubated for 60 min at 60 °C. The metabolites were analyzed by gas chromatography (7890A GC system) coupled to mass spectrometry (5975C Inert MS system) from Agilent Technologies. Metabolites were separated with a DB35MS column (30 m, 0.25mm, 0.25 μm) using a carrier gas flow of helium fixed at 1 ml/min. A volume of 1 μL of sample was injected with a split ratio 1 to 3 or spitless with an inlet temperature set at 270 °C. Polar metabolites were analyzed using a gradient started at 100°C for 1 min ramped to 105°C at 2.5°C/min, then to 240°C at 3.5°C/min and finally to 320°C at 22°C/min. For the measurement of metabolites by mass spectrometry, the temperatures of the quadrupole and the source were set at 150°C and 230°C, respectively. MATLAB was used to extract mass distribution vectors and integrated raw ion chromatograms. The natural isotopes distributions were corrected considering a combination of the theoretical mass distribution vectors (MDVs) for all potentially labeled isotopologues of a metabolite (Fernandez et al., 1996). This approach was applied by solving a linear system of equations $(\vec{X}_m = \vec{X} \cdot \bar{\bar{L}})$ where $\vec{X}_m$ and $\vec{X}$ are the measured and actual MDVs for a metabolite, and the j^{th} row of the matrix $\bar{\bar{L}}$ contains the theoretically predicted MDV for the j^{th} labeled isotopologue. The peak area was subsequently normalized to the protein content of the sample and to the internal standard glutaric acid. Data is presented as normalized mass isotopologue.

Compartment specific-metabolic measurements

To separate the mitochondrial metabolic content from the cytosolic metabolic content, selective permeabilization of the cytosolic membrane using digitonin was used as previously described (Nonnenmacher et al., 2019; Rinaldi et al., 2021). Briefly, cells were seeded in 10 cm dishes to be 80% confluent after 48h. After 24h from the seeding, the medium was replaced with one containing antimycin A + 2mM Sodium Pyruvate for overnight incubation. After, the media was replaced and cells were incubated with the corresponding labelling media. Once the pulse was done, the supernatant was removed and cells were washed with 2 mL of PBS.

Permeabilization of the cytosolic membrane was achieved by incubation with 500 μl digitonin solution at 200 μg/ml in mitochondrial assay buffer (70 mM sucrose, 220 mM mannitol, 10 mM KH_2 PO4, 5 mM $MgCl_2$, 2 mM HEPES, 1 mM EGTA, 0.2 % (w/v) fatty acid-free BSA, pH 7.2) at 37 °C for 5 min. Afterward, supernatants containing the cytosolic components were collected and stored at −80°C, while the 10 cm dishes containing the intact mitochondrial component were washed once with two volumes of saline, quenched in liquid nitrogen and stored at −80°C until metabolite were extracted as already described.

Glutamate dehydrogenase activity assay

GDH activity was measured in a coupled enzymatic assay using bovine glutamate dehydrogenase (GDH, Sigma-Aldrich G2626). Reactions were performed in 100 μL of 10 mM HEPES buffer, pH 7 at room temperature. Each reaction contained 10 mM glutamate (Sigma-Aldrich G1626), 2 mM ADP (Sigma-Aldrich A5285) and 0.1 unit of glutamate dehydrogenase. In each reaction, the ratios of NADH: NAD^+ were varied as follows: reaction 1: 230 uM NAD^+; 30 uM NADH; reaction 2: 200 uM NAD^+; 60 uM NADH; reaction 3: 170 uM NAD^+; 90 uM NADH; reaction 4: 140 uM NAD^+; 120 uM NADH; reaction 5: 110 uM NAD^+; 150 uM NADH ADH0 uM n 5: 110 uM NAD^+; 180 uM NADH; reaction 7: 50 uM NAD^+; 210 uM NADH ADH0 uM n 7: 50 uM $NADD^+$; 240 uM NADH. After 5 minutes reaction time, 20 μL of the reaction was removed and quenched with 800 μL of 50% methanol/30% acetonitrile/20% H_2O. The reactions were then analysed using mass spectrometry.

Measurement of NAD^+/NADH

To measure whole cellular NAD^+ and NADH levels, the NAD/NADH Glo Assay kit (Promega) was used following an optimized protocol from the manufacturer instructions. Briefly, 200,000 cells were seeded in 6-well plates. 24h after, media was replaced, and treatments were added and incubated for 24h. After, wells were washed with saline and quenched in liquid nitrogen. Then, cells were extracted in 1% Dodecyltrimethylammonium bromide (DTAB) in NaOH/PBS (0.5 ml/well). To measure NAD^+, 50 ul of each sample were mixed 50ul with 25ul 0.4N HCl. To measure NADH, 50 ul of each sample were separated in a different tube. All samples were incubated at 60°C for 15 min and then equilibrated to room temperature. 25ul of Tris base (0.4N) were added to the NAD^+ tube and 50ul of 1:1 HCl/Tris to the NADH tube. After vortex, 30ul of the NAD and 30ul of the NADH tubes were added to a white 96-well plate and mixed with the luminescence mixture of the kit. After 30min, the plate was measured for luminescence.

Measurement of reactive oxygen species (ROS)

Evaluation of intracellular general and mitochondrial ROS was performed using the fluorescent probes chloromethyl-2′,7′-dichlorodihydrofluorescein diacetate, acetyl ester (CM-H2DCFDA, Invitrogen C6827) and MitoSOX Red respectively. Briefly, 50,000 cells were seeded in 24-well plates and 24 h after antimycin A treatment and metabolic rescues were added. After 24h, cells were incubated with DMEM without FBS containing either CM-H2DCFDA (5 μM) or MitoSOX (5 μM) at 37°C for 30 min. Cells were then harvested by trypsinization and washed twice with PBS. Cells were suspended in PBS and analysed by flow cytometry (BD LSRFortessa™ X-20). Data analysis was conducted using FlowJo™ v10 Software.

RNA extraction, cDNA synthesis and quantitative PCR

Total RNA from biological triplicates was isolated using miRNeasy extraction kit (Qiagen) and quantified using a NanoDrop 2000c spectrophotometer (Thermo). Single-strand cDNA synthesis was performed using oligo dT-adaptor primers and the Transcriptor First Strand cDNA synthesis kit (Roche) according to the manufacturer's protocols, starting with 500 to 1000 ng of RNA. The cDNA was amplified with gene-specific primers (MDH1 Forward GGTGCAGCCTTAGATAAATACGC, Reverse AGTCAAGCAAC TGAAGTTCTCC; MDH2 Forward TCGGCCCAGAACAATGCTAAA, Reverse GCGGCTTTGGTCTCGATGT, SDHB Forward GGATC TTGTTCCCGATTTGAGC, Reverse CGTCCAGTTTCTCACGCTCT) and Fast SybrGreen in the 7900HT system (Applied Biosystems). In each assay, 30 ng of cDNA per reaction were used, including non-template-controls and samples were run in technical triplicates. The mRNA expression in each sample was normalized to β-actin. $2-\Delta\Delta Ct$ method was used to determine the relative gene expression levels, normalized to mRNA enconding actin protein (Livak and Schmittgen, 2001).

Western Blot

Total cellular proteins were extracted with RIPA buffer containing protease and phosphatase inhibitors and incubated for 10 min in ice. After centrifugation at 15,000 rpm at 4°C for 10 min, the supernatants were recovered. To separate mitochondrial and cytosolic proteins, cells were incubated in mitochondrial isolation buffer (0.25M sucrose, 1mM EDTA, 20mM HEPES, protease and phosphatase inhibitors pH 7.4) and next disrupted with 20 strokes using a Dounce homogenizer. Upon a first centrifugation at 1000g for 10min at 4°C, supernatants were taken and centrifuged again at 15000g for 10 minutes at 4°C to separate the mitochondrial and cytosolic fraction. Supernatants were collected as cytosolic proteins and the purified mitochondrial pellets were extracted using RIPA buffer containing protease and phosphatase inhibitors by incubation in ice for 10 min. After centrifugation at 15000 rpm at 4°C for 10 min, the supernatants were recovered as mitochondrial proteins. Protein concentration was measured using a Pierce BSA protein assay kit (ThermoFisher). A total of 20 μg proteins were diluted in 4× Laemmli buffer (Bio-Rad) and heat-shock treated during 10 minutes at 95°C. Proteins were resolved by sodium dodecyl sulfate polyacrylamide gel electrophoresis (SDS-PAGE) and transferred to polyvinylidene difluoride membranes (PVDF) (BioRad). Membranes were blocked with Tris-buffered saline-Tween 20 (TBST, 0.1% Tween 20) containing 5% low-fat milk (room temperature during 1 hour) and incubated at 4°C shaking overnight with the following primary

antibodies: anti-PHGDH (HPA021241, Merck Sigma), anti-TOM20 (42406S, Cell Signaling Technology), anti-CYTOCHROME C (556433, BD Pharmingen) anti-GOT2 (A304-356A-T, Bethyl laboratories), anti-MDH1 (BS-3996R, Bioss Inc.), anti-MDH2 (11908S, NEB), anti-TUBULIN (2144S, Cell Signaling Technology), anti-RPL28 (16649-1-AP, Proteintech), anti-FLAG® M2 (F1804, Merck Sigma), anti-VINCULIN (4650, Cell Signaling Technology) and anti-VDAC1 (sc-390996, Santa Cruz biotechnology). After incubation with appropriate secondary peroxidase-conjugated antibodies, signal was detected with the SuperSignal West Pico Chemiluminescence Kit (ThermoFisher) and acquired by LAS4000 system (General electric).

QUANTIFICATION AND STATISTICAL ANALYSIS

Details on statistical tests and post-tests of each experiment are presented in the figure legends. Data are presented as the mean and error bars represent standard deviation (SD) unless otherwise specified. Sample size (n) indicates the experimental replicates from a single representative experiment. Sample size for all experiments was chosen empirically. The results of experiments were validated by $\geq$3 independent repetitions. Graphs and statistical difference data were performed using GraphPad Prism 9.1.0 (GraphPad software Inc., USA). Statistical significance was determined using Student's t-test in paired groups of samples with known median and ordinary one-way analysis of variance (ANOVA) with Dunnett's or Holm-Sidak's multiple comparison test or two-way ANOVA with a Tukey's post-hoc multiple comparison test in comparison of more than two groups of samples. A p-value of $\leq$ 0.05 is considered significant (*p<0.05, **p<0.01, ***p<0.001, ****p<0.0001).